From Legacy Finite Element Modeling to Explainable Simulation: Technical Requirements for XAI in Computational Mechanics

Barna Szabó[1]

Abstract

This paper establishes technical requirements for explainable artificial intelligence (XAI) in computational mechanics, with an emphasis on controlling both the model-form and discretization errors in finite element analysis. We argue that explanation accuracy and the identification of knowledge limits—central requirements of XAI—can be satisfied only when these error sources are systematically estimated and controlled.

A model-centric framework is developed in which hierarchical discretization and model hierarchies enable traceability of modeling assumptions and quantitative assessment of their impact on quantities of interest. The approach is illustrated through numerical studies of the stability and post-buckling behavior of spherical and hemispherical shells.

The results indicate that achieving XAI in engineering requires a transition from legacy element-centric implementations to formulations grounded in the science of finite element analysis, with important implications for software architecture and simulation workflows.

Keywords: numerical simulation, solid mechanics, hierarchical shell models, model form errors, XAI integration

1. Introduction

In the evolutionary development of the finite element method, two distinct lineages emerged: the engineering practice of finite element modeling, which has its roots in the 1960s, and the mathematical theory of finite element analysis, which began to take shape about a decade later. By the 1980s, finite element analysis had matured into a formal branch of applied mathematics, while finite element modeling had become deeply embedded in engineering workflows. This evolution is now entering a new era, in which simulation processes are integrated with artificial intelligence (AI) procedures.

AI systems designed to support automated or semi-automated engineering workflows rely on mathematical models to estimate the response of physical objects or systems to various excitations. These models serve as evidence generators, producing the data upon which critical decisions are based. In this context, explainable artificial intelligence (XAI) has emerged as a fundamental requirement. It is self-evident that XAI remains unattainable if the models producing this evidence are themselves unexplainable—a reality that imposes rigorous technical requirements on how mathematical models must be formulated and applied.

[1] Department of Mechanical Engineering and Materials Science, Washington University, St. Louis, Missouri USA. szabo@wustl.edu

The software architecture of legacy finite element implementations was developed under severe constraints imposed by a then-immature understanding of the theoretical foundations and by the limited computational resources available at the time. As a result, legacy finite element codes remain architecturally centered on element libraries based on formulations that combine model definition with discretization. Although these approaches have been useful for many engineering applications, they pose fundamental difficulties when explanatory accuracy, traceability, and explicit knowledge limits must be established. Specifically, the lack of systematic control over discretization and model-form errors limits the ability to determine the reliability of predictions.

Advances in the science of finite element analysis enable *a posteriori* error estimation, and model hierarchies allow the systematic control of model-form errors. Together, these developments allow numerical simulation to satisfy key XAI requirements—specifically, that computed results be accompanied by a detailed explanation of the underlying simulation process. The objective of this paper is to make these connections explicit. We argue that satisfying the technical requirements of XAI in computational mechanics necessitates a transition from element-centric to model-centric formulations and the application of the science of finite element analysis in place of the prevailing practice of finite element modeling.

To make these ideas concrete, we focus on stability and post-buckling analyses of thin-walled shell structures. Shell buckling is a particularly demanding class of problems, involving eigenvalue multiplicity, geometric and material nonlinearity, and pronounced sensitivity to imperfections. These features make shell problems a stringent test of explanation accuracy. A fully three-dimensional variational formulation is adopted as the reference model, from which reduced representations may be derived as special cases. This approach avoids the kinematic restrictions inherent in classical shell theories while retaining the ability to control approximation errors through hierarchical finite element spaces.

1.1 Contributions of this work.

This paper makes five contributions: (i) It establishes a formal connection between the requirements of explainable AI and the components of mathematical modeling in computational mechanics, emphasizing explanation accuracy and knowledge limits. (ii) It demonstrates model-centric formulations grounded in the science of finite element analysis. (iii) It presents a fully three-dimensional formulation for stability and stress stiffening that subsumes classical plate and shell theories and supports hierarchical control of discretization and model form errors. (iv) Introduces a stabilization algorithm that supports explainability. (v) Through spherical and hemispherical shell benchmarks, it shows how hierarchical discretization, model hierarchies, and verification procedures enable explainable simulation and provide a basis for XAI-native engineering workflows.

1.2 Organization of this paper

The paper is organized as follows. Section 2 summarizes the technical requirements of explainable AI relevant to numerical simulation. Section 3 introduces a conceptual framework for model development that distinguishes among discretization errors, model form errors, and calibration errors, and relates these to explanation accuracy and knowledge limits. Section 4 places these issues in an evolutionary context. Section 5 presents a three-dimensional formulation for stability and stress stiffening that subsumes classical formulations. Sections 6–8 provide numerical examples involving bifurcation buckling and the imperfection sensitivity of thin spherical and hemispherical shells, illustrating how hierarchical modeling and verification support explainable simulation. A new stabilization algorithm is introduced in

Section 7.1. The paper concludes with a discussion of uncertainty and the implications of these results for the future integration of computational mechanics with AI-based workflows.

2. The requirements of XAI

The requirements that define explainable AI are stated in a 2021 National Institute of Standards and Technology (NIST) report [1] as follows:

a) **Explanation** — The system provides accompanying evidence, support, or reasoning for its outputs and/or processes (not just the result, but why it reached that conclusion).
b) **Understandable** — Explanations must be tailored and comprehensible to the individual user.
c) **Explanation accuracy** — The provided explanation must correctly and faithfully reflect the process the system used to generate the output.
d) **Knowledge limits** — The system only operates within the conditions for which it was designed, and it communicates its own limitations (e.g., refuses to predict when data or parameters lie outside of the domain of calibration).

For a recent survey on the applications and expected future directions of XAI, we refer to [2]. Here, we focus on the development of XAI-native algorithms in solid mechanics. By this, we mean algorithms whose design inherently incorporates interpretability and explainability as primary objectives, rather than treating explanation as a post hoc step.

To understand how the requirements of explanation accuracy and knowledge limits apply to numerical simulation, we need a high-level description of what a mathematical model is and to establish the relevant terminology. This is discussed next.

3. Mathematical models

A mathematical model is a transformation of one set of data $\boldsymbol{D}$, the input, into another set, the quantities of interest $\boldsymbol{F}$, subject to certain constraints:

$$\boldsymbol{D} \xrightarrow[(I,\,\boldsymbol{p})]{} \boldsymbol{F} \Longrightarrow \boldsymbol{F}_{num}, \quad (\boldsymbol{D},\boldsymbol{p}) \in \mathbb{C}, \quad |\boldsymbol{F} - \boldsymbol{F}_{num}| \leq \tau|\boldsymbol{F}| \tag{1}$$

where the right arrow represents the mathematical model, which consists of a set of operators. For example, a mathematical model formulated to predict the fatigue life of a mechanical component subject to high-cycle fatigue comprises three operators: one that solves an elasticity problem, one that predicts the onset of failure given a load spectrum, and one that accounts for the statistical dispersion of failure events [3].

The letters $(I, \boldsymbol{p})$ indicate that the transformation involves an idealization I and a set of parameters $\boldsymbol{p}$ that are determined by calibration. Restrictions on $\boldsymbol{D}$ and $\boldsymbol{p}$, arising from the assumptions incorporated in the mathematical model and from the experimental data available for calibration, define the **domain of calibration** $\mathbb{C}$.

The exact value of $\boldsymbol{F}$ is not known, only an approximate value, computed by a numerical method, $\boldsymbol{F}_{num}$ is known. It is necessary to ensure that the error of $\boldsymbol{F}_{num}$ is within allowable bounds.

The predictive performance of a mathematical model is influenced by three types of error: model-form errors arising from the assumptions used in formulating the model operators, discretization errors

resulting from the numerical approximation of partial differential equations, and experimental errors in parameter calibration. Accordingly, the requirement of explanation accuracy is satisfied only when all three error types are estimated and controlled.

The requirement to establish knowledge limits is satisfied through the domain of calibration. This constitutes an essential component of any mathematical model. A mathematical model is considered validated when the $\boldsymbol{D}$ and $\boldsymbol{p}$ lie in the domain of calibration.

4. The evolving objectives of model development

As advances in theory and computing have removed many of the constraints that once shaped engineering practice, the goals of model development today differ markedly from those of the pre-computer era. The evolution of plate and shell models provides a clear illustration of how these objectives have changed over time. To demonstrate how model development has been driven by advances in scientific knowledge, computational capabilities, and, more recently, artificial intelligence, the progression of plate and shell models is traced across three distinct periods.

4.1 The Classical Period (late 1890s to 1960s)

In formulating classical plate and shell models, the goal was to find an approximation to the solution of a fully three-dimensional theory of elasticity problem on domains of small thickness. Dimensional reduction was used for this purpose; that is, the problem was recast such that the 3D problem of elasticity could be solved on two-dimensional domains—typically the mid-surface of a plate or shell. To achieve this, four types of assumptions were introduced:

a) assumptions regarding the mode of deformation (e.g., neglecting shear deformation),
b) assumptions about constitutive relationships
c) assumptions concerning idealization of loading
d) assumptions concerning idealization of kinematic boundary conditions.

In 1959, Morgenstern showed that the stresses and strains obtained from solutions of Kirchhoff's plate theory converge, in a mean-square sense, to the corresponding solutions of three-dimensional elasticity as the plate thickness approaches zero [4]. This result provided the first rigorous justification of the Kirchhoff model as the correct asymptotic limit of 3D elasticity for vanishing thickness. Similar convergence results were later established for Reissner–Mindlin plate models [5]. For finite plate thicknesses, however, the underlying assumptions introduce model-form errors, that is, errors inherent in the formulation itself.

4.2 The pre-science period (1960s and 70s): Element-centric development

There was a surge of interest in matrix methods applied to elasticity and, more generally, continuum mechanics during the 1960s and 1970s. The focal point of this activity was a series of three international conferences held at Wright-Patterson Air Force Base in Dayton, Ohio. The first of these conferences (26–28 October 1965) addressed plate and shell elements, stiffness matrices, convergence, and large-scale structural applications. The proceedings of this meeting [6] provide a representative survey of the state of the art at that time. In the same year, NASA issued a request for proposals for the development of a general-purpose finite element structural analysis program, which ultimately led to NASTRAN and served as a prototype for other legacy finite element codes still in use today.

According to Thomas Kuhn, a pre-science period is marked by the absence of a common conceptual framework—no shared assumptions, no standard methods, and no consensus about what constitutes a valid model [7]. Instead, development proceeds largely by trial and error. — This is a fair characterization of engineering research on the finite element method in the 1960s and 1970s. The focus of the investigation was element-centric, with the goal of defining finite elements whose stiffness approximated that of the corresponding plate, shell, or solid segment as defined by classical theories.

The early development of the finite element method proceeded under two severe constraints. The first was an incomplete understanding of its theoretical foundations. As evidenced in [6], much of the early work relied on intuitive, trial-and-error approaches typical of engineering practice when confronting a new problem. The second constraint was the severe limitation of available computational resources. For example, solving a dense 200 × 200 eigenvalue problem required out-of-core techniques or reduced-basis methods, even on the most advanced computers of the era, such as the CDC 6600 or the IBM 7094. These constraints imposed significant restrictions on algorithm design, software architecture, and element formulations.

By the time advances in theory and computing power had removed these limitations, finite element codes had become firmly embedded in engineering practice, and any substantive change would have required major revisions. The solvers and user interfaces were regularly updated, but the underlying element formulations—and the many technical limitations associated with them—remained largely untouched. As a result, *constraints that no longer exist continue to handicap legacy finite element codes*.

4.3 The Period of Normal Science (mid-1970s to present): Model-centric Development

According to Thomas Kuhn, the period of normal science begins when a paradigm has been established and accepted by a scientific community. In the context of the finite element method, this period began in the 1970s and continues to the present day. During this time, scientific inquiry focused on the adaptive control of discretization errors and later progressed toward the control of model-form errors through the use of model hierarchies. We now have the ability to control both discretization errors and model-form errors [8]. This is an essential prerequisite for integrating numerical simulation with XAI.

Given our computational power today, we can model plates and shells as fully three-dimensional objects and to control model form errors not only by relaxing restrictive assumptions about deformation modes but also by removing the assumption of linear material behavior. In the interest of numerical efficiency, we will employ anisotropic finite element spaces in our examples.

Our goal in model development has shifted from using simplifying assumptions to make the problem tractable with classical methods to controlling model-form errors. In other words, the original reasons for creating classical plate and shell models no longer exist.

5. Formulation

We consider the elastic stability of a fully three-dimensional body and construct a mathematical model free of the various restrictions inherent in beam, plate, or shell models. From this model, various dimensionally reduced models can be derived as special cases, allowing, at least in principle, the selection of the simplest model that accounts for all features that significantly influence the quantities of interest.

We will use a total Lagrangian formulation assuming small strains, while placing no restrictions on the magnitude of displacements or rotations. By small strains, we imply that the non-linear product terms in the Green-Lagrange strain tensor are negligible in comparison with the linear terms within a suitably rotated local frame. Index notation will be employed throughout.

We assume that a three-dimensional elastic body in its reference configuration Ω is subjected to an initial stress field σ_{ij}^0 which satisfies the equations of equilibrium of linear elasticity:

$$\sigma_{ij,j}^0 + F_i^0 = 0, \quad \sigma_{ij}^0 n_j = T_i^0 \; on \; \partial\Omega_T \tag{2}$$

where F_i^0 is the body force, n_j is the unit normal to the boundary surface, $\mathrm{T_i^0}$ is the prescribed traction vector, and $\partial\Omega_T$ is that part of the boundary surface where tractions are prescribed. Assuming homogeneous essential boundary conditions, the generalized form is:

$$\frac{1}{2}\int_\Omega \sigma_{ij}^0 \left(v_{i,j} + v_{j,i}\right) dV = \int_\Omega F_i^0 \, v_i \, dV + \int_{\partial\Omega_T} T_i^0 v_i \, dS\,, \qquad v_i \in E^0(\Omega) \tag{3}$$

where $E^0(\Omega)$ denotes the space of functions that lie in the energy space and vanish on those boundary segments where essential boundary conditions are prescribed. Equation (3) can be understood to mean that when the body in equilibrium is subjected to a virtual displacement v_i the virtual work of external forces equals the virtual work of internal stresses.

The Green strain tensor (also known as the Green-Lagrange finite strain tensor) is a measure of finite strain in continuum mechanics. It is defined in terms of the gradient of the displacement vector relative to the reference configuration as follows:

$$E_{ij} = \frac{1}{2}\left(u_{i,j} + u_{j,i} + u_{m,i}u_{m,j}\right) \tag{4}$$

Let us assume that the loading of the body is changed through the imposition of increments of body force F_i, surface traction T_i and/or a spring displacement d_i imposed on linear (Winkler) springs characterized by the coefficients k_{ij} and defined on boundary segment $\partial\Omega_s$. The strain energy is defined by

$$U(u_i) \; = \; \frac{1}{2}\int_\Omega C_{ijkl}\varepsilon_{ij}\varepsilon_{kl} dV + \frac{1}{2}\int_{\partial\Omega_s} k_{ij}u_i u_j dS + \frac{1}{2}\int_\Omega \sigma_{ij}^0 \, u_{m,i}u_{m,j} dV \tag{5}$$

where C_{ijkl} is the tensor of material properties. The third term corresponds to the work done by σ_{ij}^0 through the product term of the Green strain tensor. The work done through the linear terms vanishes on account of Equation (3). The potential energy is:

$$\Pi(u_i) = \; U(u_i) \; - \int_\Omega F_i \, u_i dV - \int_{\partial\Omega_T} T_i u_i dS - \int_{\partial\Omega_s} k_{ij}u_i \mathrm{d}_j dS \tag{6}$$

The effect of the initial stress σ_{ij}^0 depends on its sense and magnitude: If it is predominantly positive (i.e., tensile), then the stiffness increases. This is called stress stiffening. If, on the other hand, σ_{ij}^0 is predominantly negative, then the stiffness decreases. Of great practical interest is the critical value of the initial stress at which the stiffness is zero.
Define:

$$\sigma_{ij}^{0} = \lambda \hat{\sigma}_{ij} \tag{7}$$

In stability problems, $\hat{\sigma}_{ij}$ is the pre-buckling stress field. We define the bilinear form

$$B_{\lambda}(u_i, v_i) = B(u_i, v_i) - \lambda G(u_i, v_i) \tag{8}$$

where

$$B(u_i, v_i) = \int_{\Omega} C_{ijkl}\, u_{i,j} v_{k,l}\, dV + \int_{\partial\Omega_s} k_{ij} u_j v_i\, dS \tag{9}$$

$$G(u_i, v_i) = -\int_{\Omega} \hat{\sigma}_{ij} u_{m,j} v_{m,i}\, dV \tag{10}$$

The problem is to find u_i in the space of admissible functions such that

$$B_{\lambda}(u_i, v_i) = \mathcal{F}(v_i) \quad \text{for all } v_i \in E^0(\Omega) \tag{11}$$

where

$$\mathcal{F}(v_i) = \int_{\Omega} F_i v_i dV + \int_{\partial\Omega_T} T_i v_i dS + \int_{\partial\Omega_s} k_{ij} d_j v_i dS \tag{12}$$

The set of λ for which Equation (11) is uniquely solvable for all $\mathcal{F}$ is called the *resolvent set*. The complement of the resolvent set is the *spectrum*. In addition to the point spectrum, which consists of the eigenvalues λ_i $(i = 1, 2, \dots)$ the spectrum may also include values that lie in a *continuous spectrum*. Fortunately, in engineering problems that require consideration of the stability of thin-walled elastic structures, the smallest values of λ belong to a *point spectrum* and these eigenvalues can be reliably approximated using the finite element method without pollution by spurious modes [9].

The minimum of the potential energy is found by iteration. The geometric configuration is updated at each step.

6. Example: Bifurcation buckling of spherical shells

In this example, we show that the lowest eigenvalue predicted by the mathematical model described in the preceding section coincides with that obtained from the classical formulation, which admits only axially symmetric eigenfunctions. However, in the present formulation, this eigenvalue is observed to have a large, possibly infinite, multiplicity.

In bifurcation buckling problems, we seek the minimum of λ such that $B_{\lambda}(u_i, v_i) = 0$ has a nontrivial solution. Here, we consider a perfect sphere subjected to uniform external pressure. The critical value of this pressure, denoted by P_{cr}, was estimated in 1915 in a doctoral dissertation by R. Zoelly and discussed in [10]. The estimate is based on the assumptions of the Kirchhoff-Love shell theory: (a) normals to the mid-surface in the undeformed configuration remain straight and normal after deformation, (b) the stress component normal to the mid-surface can be neglected, (c) the thickness does not change, and (d) the strains and rotations are small. Furthermore, it was assumed that the buckling deformation is axially symmetric, that is, it can be described as a function of the polar angle only.

For this example, we will use the following geometric and material properties: The mean radius of the shell is $R = 100$ mm and the thickness is $t = 1.0$ mm. The material is assumed to be isotropic and elastic with Young's modulus 200 GPa and Poisson's ratio 0.3. Given these properties, the predicted critical pressure is:

$$P_{cr} = \frac{2E}{\sqrt{3(1-\nu^2)}}\left(\frac{t}{R}\right)^2 = 24.21 \text{ MPa} \tag{13}$$

We have sufficient computational resources to treat the shell as an elastic body. We do not need to make the a priori assumption that the first buckling mode is axisymmetric, allowing the model to capture asymmetric buckling modes. The model is also suitable for investigating post-buckling behavior for both linear and nonlinear materials, as discussed in the following section.

We discretized a sphere using 64 triangular and 128 quadrilateral shell elements, shown in Figure 1(a). The mapping functions were fifth-degree polynomials defined on the Chen-Babuška collocation points [11]. Converging sequences of approximate solutions were obtained using the anisotropic finite element spaces $S(\Delta, p, p, q)$ where Δ represents the mesh, and p represents the polynomial degree of the displacement functions in the tangential directions of the mid-surface, and q represents the polynomial degree in the transverse direction. We present results for a 192-element mesh shown in Figure 1, with p ranging from 5 to 8 and q = 3, 5. The computations were performed with StressCheck[2].

Rigid body constraints were enforced by modifying the boundary conditions to impose a very weak spring constraint on the entire surface of the sphere. Specifically, the bilinear form in eq. (9) was defined as follows:

$$B(u_i, v_i) = \int_\Omega C_{ijkl}\, u_{i,j} v_{k,l}\, dV + k \int_{\partial\Omega_s} \delta_{ij} u_j v_i\, dS \tag{14}$$

where $k = 10^{-3}$ MPa/mm and δ_{ij} is the Kronecker delta. Given the size of the modulus of elasticity, and noting that the pre-buckling stress is of order 1, this choice of k introduces a negligibly small error in the computed value of the critical pressure.

The computed values of the critical pressure are shown in Table 1. The numerical results show that the computed values monotonically converge to a limit slightly below the value given in Equation (4). The convergence must be monotonic with respect to increasing degrees of freedom, since the critical values are obtained by minimizing the Rayleigh coefficient over a hierarchical sequence of approximation spaces.

Table 1: The computed values of P_{cr}.

p	q = 3			q = 5		
	DoF	P_{cr} (MPa)	ERE (%)	DoF	P_{cr} (MPa)	ERE (%)
5	18,360	24.14	0.78	19,332	24.14	0.78
6	27,384	24.07	0.08	29,412	23.97	0.08
7	38,712	23.95	0.00	43,044	23.95	0.00
8	52,344	23.95	0.00	59,748	23.95	0.00
Est.d limit:		23.95			23.95	

[2] StressCheck is a registered trademark of Engineering Software Research and Development, Inc.

To our knowledge, the multiplicity of the eigenvalues of spherical shells has not been analyzed in the non-compact setting. The numerical results indicate that the computed eigenvalues are very closely spaced: the difference between the first and the 50th eigenvalues is only 0.36%, and between the first and the 100th is 0.86%. These findings do not rule out the possibility that this spread is due to numerical error, and that the lowest exact eigenvalue(s) have high—possibly infinite—multiplicity.

The lowest nonzero eigenvalue appears to be of multiplicity two, and the corresponding eigenfunctions are shown in Figure 3. These eigenfunctions are clearly non-axisymmetric. However, the classical solution—based on the assumption of axisymmetric eigenfunctions—yields an eigenvalue remarkably close to the estimated limit given in Table 1. A possible explanation is that the first eigenvalue has a larger multiplicity, and the associated eigenspace contains, among others, the first axisymmetric mode.

Remark: The eigenfunctions shown in Figures 1(b) and 1(c) display a pattern that favors the pole. The third eigenfunction (not shown) is perfectly axisymmetric with respect to the pole. Since the pole is an artifact of the finite element mesh shown in Figure 1(a), this has to be a mesh-dependent phenomenon. This was confirmed by repeating the computations with an automatically generated unstructured mesh of quadrilateral and triangular elements that had no pole. The normal displacement exhibited no recognizable pattern; however, the eigenvalues had a large apparent multiplicity and were substantially independent of the finite element mesh.

When an eigenvalue has a multiplicity of two or more, any computed eigenfunction is not unique; it is only guaranteed to lie within the corresponding eigenspace and depends on the particular basis chosen by the solver, which is discretization-dependent. This non-uniqueness of the basis explains why the computed eigenfunctions depend on the choice of discretization [12].

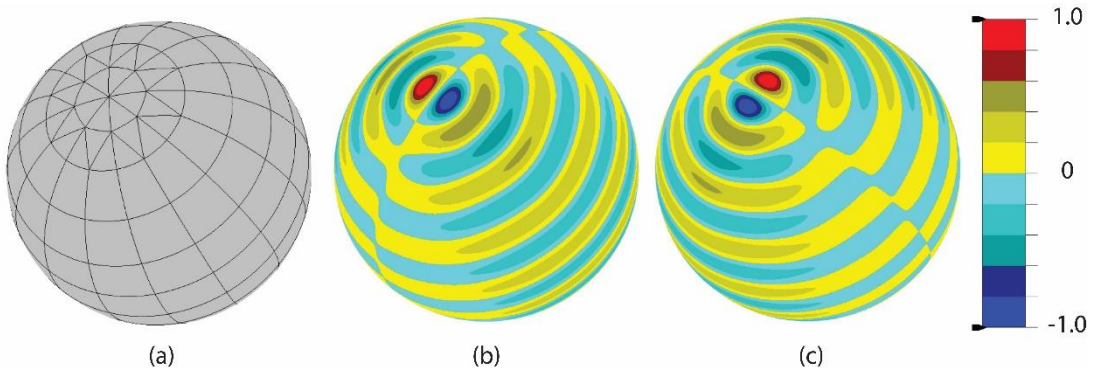

Figure 1: (a) Finite element mesh consisting of 192 elements. (b) The first buckling mode. (c) The second buckling mode. The contours represent normal displacements.

Remark: The 192-element mesh shown in Fig. 1(a) was created to explore the multiplicity of eigenvalues in the vicinity of the smallest eigenvalue. The usual goal of computation is to estimate the smallest eigenvalue. This problem can be solved with significantly fewer elements and, therefore, a much smaller number of degrees of freedom. For example, using a 48-element mesh, the predicted limit value differs from that reported in Table 1 by only 0.3%.

6.1 Explainability and Knowledge Limits

Suppose two analysts solve an eigenvalue problem using different discretizations, and the eigenvalue has multiplicity at least 2. They will agree on the eigenvalues but will very likely disagree on the mode shapes. The explanation is based on reference [12], which shows that, for multiple eigenvalues, the mode shapes are not uniquely defined.

This example illustrates how hierarchical discretization satisfies a key XAI requirement. Explanation accuracy is supported by the monotonic convergence of the critical pressure with respect to the hierarchical spaces $S(\Delta, p, p, q)$, allowing estimation of the relative error (ERE in Table 1) and demonstrating that the computed data are substantially independent of the discretization.

7. Example: Post-buckling of a perfect hemispherical shell

In this section, we address aspects of controlling model-form errors. We consider the post-buckling behavior of a perfect hemispherical shell of radius 100 mm, thickness 1.0 mm, subjected to uniform normal pressure (a follower load). The equatorial plane is a symmetry plane. The goal of computation is to estimate the coordinates of the limit point on the equilibrium load path.

We will consider two material models: (a) isotropic and elastic material with Young's modulus 200 GPa and Poisson's ratio 0.3 (the same as in the previous example), and (b) elastic-plastic behavior based on the deformation theory of plasticity (Hencky's total strain theory) with the material behavior represented by the Ramberg-Osgood equations. In the complete tensorial form:

$$\epsilon_{ij} = \frac{1+\nu}{E} s_{ij} - \frac{1-2\nu}{3E}\sigma_{kk}\delta_{ij} + \frac{3}{7}\left(\frac{S_{70E}}{E}\right)\left(\frac{\sigma_{eq}}{S_{70E}}\right)^{n}\left(\frac{3}{2}\frac{s_{ij}}{\sigma_{eq}}\right) \tag{14}$$

where: ϵ_{ij} is the strain tensor; σ_{ij} is the Cauchy stress tensor; s_{ij} is the deviatoric stress tensor, σ_{eq} is the equivalent (von Mises) stress; E is Young's modulus; ν is Poisson's ratio, S_{70E} is the stress read from the uniaxial stress-strain curve corresponding to its point of intersection with a line that passes through the origin and has the slope $0.70E$ and n is a calibration parameter. In the present example, $E = 200$ GPa, $\nu = 0.3$, $S_{70E} = 1.37$ GPa, and $n = 20$.

The equivalent strain is:

$$\epsilon_{eq} = \frac{\sigma_{eq}}{E} + \frac{3}{7}\left(\frac{S_{70E}}{E}\right)\left(\frac{\sigma_{eq}}{S_{70E}}\right)^{n} \tag{15}$$

where

$$\epsilon_{eq} \equiv \left((2/3)\bar{\epsilon}_{ij}\bar{\epsilon}_{ij}\right)^{1/2}, \qquad \bar{\epsilon}_{ij} \equiv \epsilon_{ij} - (1/3)\epsilon_{kk}\delta_{ij} \tag{16}$$

One of the assumptions in our model is that the strains are small. Although there is no strict upper bound for the validity of small-strain theory, it is generally considered applicable for $\epsilon_{eq} \leq 0.01$ (1%). Larger values may be acceptable depending on the QoI and the required accuracy.

The finite element mesh, consisting of 8 triangular and 32 quadrilateral shell elements, is shown in Figure 2. The constraint conditions are as follows: On the equatorial plane, $u_z = 0$. Ideally, this plane would be a symmetry plane, hence the shearing stresses would be zero. However, to prevent rigid-body displacements, the displacement vector components in the x and y directions must be constrained. To achieve this, we introduce the weak boundary conditions: $T_x = ku_x$ and $T_y = ku_y$ where k is a small

number. In the present problem, we used $k = 10^{-4}$ MPa/mm. Therefore, it is necessary to show that the quantities of interest are substantially independent of the choice of k. This will be discussed in Section 7.3.

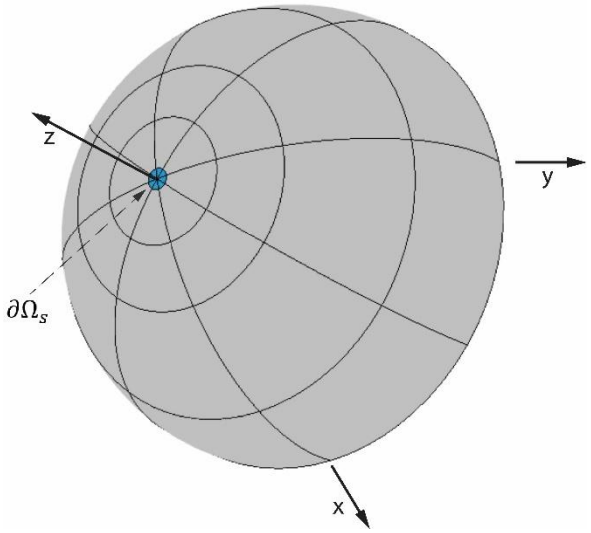

Figure 2: Hemispherical shell. Notation.

7.1 Stabilization algorithm

To stabilize the problem, we introduce a distributed spring over a small surface domain $\partial\Omega_s$, indicated by blue shading in Figure 2. This domain is bounded by a colatitude of 2.5 degrees. The loading on $\partial\Omega_s$ is modified by imposing the following Robin boundary condition:

$$T_z(\boldsymbol{x}) = k_s(d_z - u_z(\boldsymbol{x})) \qquad \boldsymbol{x} \in \partial\Omega_s \tag{17}$$

where T_z is the traction vector component in the z direction, $\boldsymbol{x}$ is the position vector, k_s is a spring rate, d_z is a displacement imposed on the spring, and u_z is a displacement vector component.

The objective is to find the normal pressure acting on the shell when the average of u_z over $\partial\Omega_s$ is equal to d_z. This constraint guarantees that the mathematical problem is uniquely solvable at any load level. Note that the influence of this constraint vanishes when the equilibrium equations are satisfied at $u_z = d_z$.

A reasonable choice for k_s is to have $u_z \cong d_z/2$ in the first iteration. To find k_s, we apply an arbitrary traction T_z^0 on $\partial\Omega_s$ with the resultant F_0, compute the average of the corresponding displacement $\bar{u}_z$ on $\partial\Omega_s$, and calculate k_s from

$$k_s = F_0/(\bar{u}_z A_0) \tag{18}$$

where A_0 is the area of $\partial\Omega_s$. For the present problem, $k_s = 100$ MPa/mm was used.

The nonlinear equations were solved using the successive substitution method, in which the stiffness matrix is recomputed at each iteration based on the current displacement field, and the out-of-balance force vector is used as the right-hand side. This algorithm was analyzed in detail by Ortega and

Rheinboldt in [13]. For root-finding, the Newton-Raphson method can be used. Experience with post-buckling analysis has shown that this algorithm is robust and efficient.

This algorithm is an alternative to the arc-length method, which was first introduced in the context of the finite element method by Riks [14]. The arc-length method constrains increments in the load–displacement space using a global spherical constraint equation, thereby overcoming the limitations of pure load or displacement control near limit points and turning points. In the arc-length method, stabilization is introduced at the level of the numerical solution procedure.

In contrast, the present algorithm incorporates stabilization directly into the mathematical model through a physically interpretable constraint (a distributed spring/Robin boundary condition). This approach ensures unique solvability while preserving consistency with the variational formulation and supports explainability, since the effect of the constraint is explicit and verifiable.

7.2 Numerical solution

The finite element space $S(\Delta, 8,8,3)$, where Δ is the 40-element mesh shown in Figure 2, was used to compute the equilibrium load paths for the hemispherical shell. The results of computation for the linear and nonlinear materials are shown in Figure 3. The reference pressure is the critical pressure given by Equation (13). The displacement is characterized by the absolute value of the average displacement

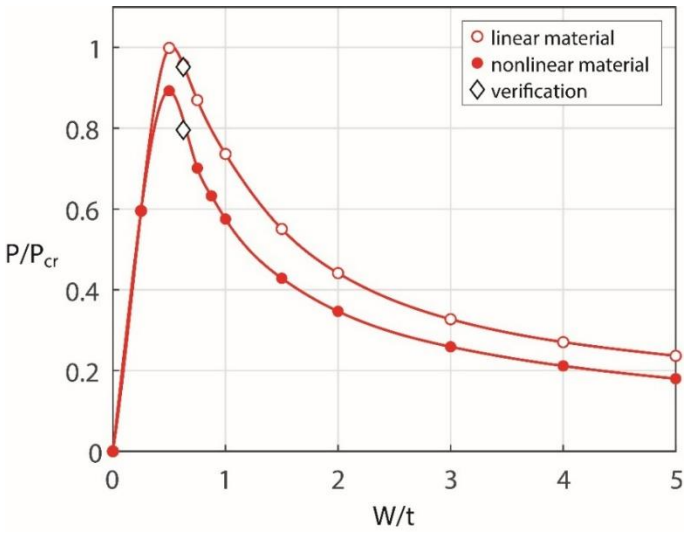

Figure 3: Equilibrium load paths for the perfect hemispherical shell.

over the domain $\partial\Omega_s$, denoted by W, and normalized with respect to the thickness t. The tolerance for the equilibrium iterations was set at 0.5% in energy norm. Given the magnitude of the critical pressure, this tolerance corresponds to an uncertainty of approximately 0.1 MPa.

The computed data points were fitted by a cubic spline using MATLAB routines, and the coordinates of the limit points were estimated from the fitted curves. The results are shown in Table 2.

This table shows that the linear material model overestimates the limit point by more that 10%. Of course, the difference between predictions based on linear and nonlinear models depends on the material properties. Therefore, this difference can be larger or smaller.

Table 2: Perfect hemispherical shell. Coordinates of the limit point.

Model	Limit point
Linear material	(0.508, 1.000)
Nonlinear material	(0.503, 0.897)

To ensure that the small-strain assumption incorporated in our mathematical model is not violated, we determine the maximum value of the equivalent strain at the limit point (0.503, 0.897). We find this value to be 0.550%, which is less than the allowable limit. Therefore, the data lie within the domain of calibration.

7.3 Explanation accuracy

Solution verification was performed by uniformly subdividing each element and increasing the polynomial degree of the transverse variation of displacements from 3 to 5. This refinement increased the number of elements from 40 to 160 and the number of degrees of freedom from 10,932 to 49,730. The computations were repeated for $W/t = 0.625$. The corresponding values of P/P_{cr} are indicated by the diamond markers in Figure 3. The results confirm that the initial choice of discretization was adequate for the purposes of the present computations.

To demonstrate that the quantities of interest are substantially independent of the choice of the spring rate k, which was introduced to prevent rigid body displacement, the computations were repeated for $k = 10^{-2}$ MPa/mm. The estimated values of P/P_{cr} at $W/t = 0.625$ differed by only 0.2%. Note that the error tolerance in equilibrium iterations was set to 0.5% of the energy norm.

8. Example: Hemispherical shell with dimple imperfections

We consider a problem discussed by Hutchinson in reference [15]. Specifically, we are interested in the buckling strength of a hemispherical shell with an imperfection in the mid-surface at the pole. The dimple is axisymmetric; the generating curve of the mid-surface of the dimpled shell is characterized by the radius

$$R = R_0 - \delta e^{-((\theta-\pi/2)/\beta)^2}, \quad 0 \le \theta \le \pi/2 \tag{19}$$

where δ and β are the depth and width of the imperfection, respectively. In this example, we use $R_0 = 100$ mm, thickness $t = 1.0$ mm, and $\beta = 5.8663^o$. The parameter β corresponds to $B = 1$ defined in equation (6.2) in reference [15]. The width of the imperfection was chosen based on the critical wavelength predicted by the classical buckling model, formulated as an axisymmetric problem. At the equator, symmetry boundary conditions are approximated by imposing $u_z = 0$, $T_x = ku_x$ and $T_y = ku_y$ where $k = 10^{-2}$ MPa/mm. The shell is subjected to uniform live pressure P. The material properties are the same as in the previous example (see Section 5).

8.1 Numerical solution

An automatic mesh generator was used to create a mesh consisting of 11 triangular and 73 quadrilateral shell elements. In the meshing process, it was enforced that the bounding circle of $\partial\Omega_s$ and the colatitude β were covered by element boundaries. The elements were mapped using the Chen-Babuska

collocation points at p=5. The anisotropic space $S(\Delta,5,5,3)$ was used, the number of degrees of freedom was 8,127.

The results of computation for the post-buckling model for the case for $\delta/t = 5.0$ are shown in Figure 4. A comparison of the curves in Figures 3 and 4 shows that the dimple reduces the estimated load-carrying capacity of the hemispherical shell by a substantial margin.

The curve taken from Figure 7(a) in reference [15] appears to combine these models incorrectly. At the origin, it exhibits the characteristics of a bifurcation model with $P/P_{cr} = 1$, as expected when no dimple exists ($\delta = 0$). It subsequently transitions to a load-displacement relationship consistent with nonlinear post-buckling models. The problem is that these models are based on different formulations, and the quantities of interest differ. Therefore, they are not directly comparable. Additionally, the abscissa uses W/t, which is not defined in the context of bifurcation buckling.

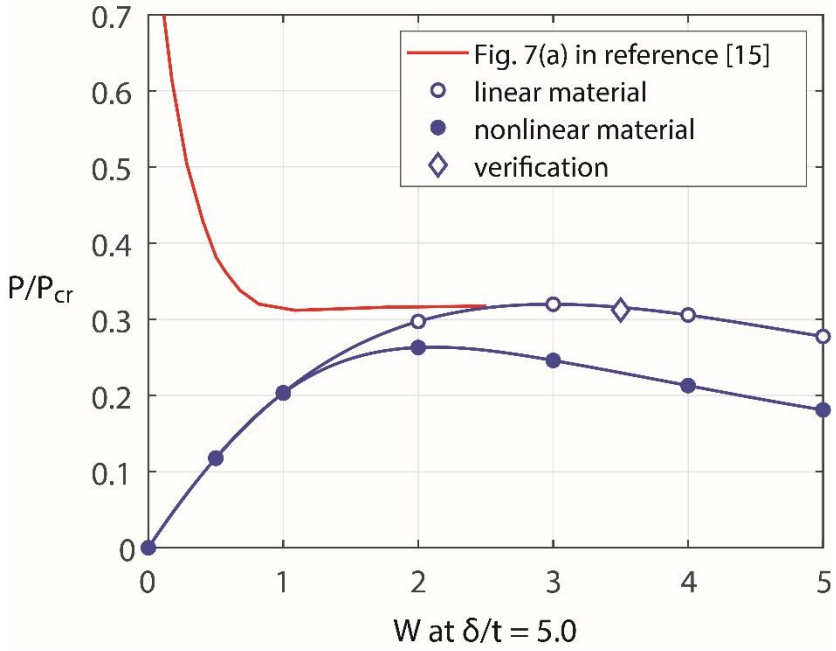

Figure 4: Dimpled hemisphere. Comparison of the equilibrium load paths predicted by linear and nonlinear material models and the load path predicted in reference [14].

The estimated coordinates of the limit points $(W/t,\ P/P_{cr})$ for the linear and nonlinear material models are presented in Table 3. The results of computation for the Ramberg-Osgood parameter n = 100 are also shown in this table for the following reason: All parameters defining a constitutive relationship exhibit statistical dispersion; however, typically only their estimated mean values are considered. Estimating the sensitivity of the quantities of interest to parameter choices is crucial in simulations. Letting n = 100 results in a very nearly elastic-perfectly plastic constitutive law. The results show that the location of the limit point is not sensitive to the choice of n.

Table 3: Estimated coordinates of the limit points at $\delta/t = 5.0$.

Model	Limit point
Linear material	(2.99, 0.320)
Nonlinear material, n = 20	(2.11, 0.263)
Nonlinear material, n = 100	(2.06, 0.266)

To ensure that the small-strain assumption incorporated in our mathematical model is not violated, we determine the maximum value of the equivalent strain at the limit point (2.11, 0.263). We find this value to be 0.183%, which is less than the allowable limit. Therefore, the data lie within the domain of calibration.

8.2 Solution verification

Solution verification is concerned with showing that the errors of approximation in the quantities of interest are within acceptable tolerances. The computations were repeated for $W/t = 3.5$ using the space $S(\Delta,8,8,3)$, which has 22,743 degrees of freedom. Although this nearly tripled the degrees of freedom, the predicted data point, indicated by a diamond marker in Figure 4, falls on the load-displacement curve. This result provides evidence that using the anisotropic space $S(\Delta,5,5,3)$ was sufficient for this model.

8.3 Imperfection sensitivity

The effects of imperfections on the location of limit points depend not only on the amplitude of the imperfection but also on its diameter and shape. This makes it difficult to quantify these effects on structural stability. To demonstrate this, we examine a dimpled spherical shell in which the dimple is represented by a cubic spline instead of the exponential curve given by Equation (19). Specifically, for $\pi/2 - \beta \leq \theta \leq \pi/2$;

$$R = R_0 - \delta(1 - 3s^2 + 2s^3), \quad s = (\pi/2 - \theta)/\beta \tag{20}$$

and $R = R_0$ for $0 \leq \theta < \pi/2 - \beta$). Figure 5 illustrates the details of the two generating curves for the imperfections analyzed here for the case $\delta = 5.0$ mm, $\beta = 5.8663°$.

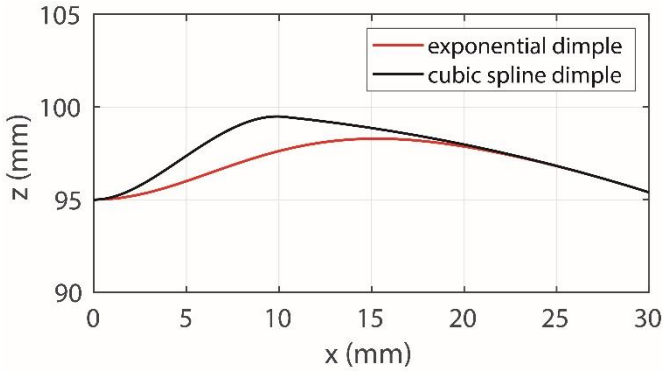

Figure 5: Details of two generating curves for the case $\delta/t = 5..0,\ \beta = 5.8663^o$.

For the dimpled shell, the space $S(\Delta,5,5,3)$ defined on an automatically generated unstructured mesh of 100 elements (16 triangles, 84 quadrilaterals) was used. The stopping criterion was based on a change of less than 0.5% in the estimated energy norm. The estimated coordinates of the limit points are shown in Table 4.

Table 4: Spline dimple. Coordinates of the limit point at $\delta/t = 5.0$.

Model	Limit point
Linear material	(1.43, 0.508)
Nonlinear material, n = 20	(1.11, 0.428)

Remark: Considering linearly elastic material only, the type of imperfection sensitivity considered here can be treated by classical shell theories. However, the effects of many other types of imperfections—such as notches, corrosion defects, cut-outs, stiffeners, and similar discontinuities—cannot be reliably modeled by classical methods. In such cases, a fully three-dimensional model, at least locally, is the proper approach.

8.4 Explainability in the post buckling example

The foregoing post-buckling analysis demonstrates how model-form errors can be controlled to satisfy XAI requirements. Explanation accuracy is supported by a fully three-dimensional formulation that avoids the restrictive assumptions of classical shell theories and enables the influence of geometric and material nonlinearities to be quantified in terms of the quantity of interest (QoI), here the limit point.

Weak boundary conditions and Robin stabilization were introduced in a manner that preserves the integrity of the mathematical model. Transparency in how constraints affect the solution is essential for generating trustworthy and explainable simulation results.

9. Uncertainties

A realistic prediction of the load–deformation response of shell structures must account for uncertainties in boundary conditions, material modeling, and various forms of imperfection. The example of dimpled hemispherical shells underscores the importance of accounting for imperfections in the analysis. This is rarely done in practice, despite the fact that observations in validation experiments are random variables. Consequently, the mathematical model should predict the probabilities of possible outcomes.

Given current computational capabilities, it is feasible to perform Monte Carlo simulations and obtain probability density estimates for quantities of interest. This approach provides a rational basis for establishing lower bounds on safety factors. However, the selection of safety factors must ultimately rely on expert consensus, as statistical models cannot reliably estimate the probability of extremely rare events. Safety factors are intended to protect against unforeseeable occurrences and events of such low probability that they cannot be empirically validated. This leads to a striking paradox: the most critical quantity in engineering—the factor of safety—cannot itself be validated.

When the goal is to estimate the load-carrying capacity of a shell, the simplifications of buckling analysis based on linearly elastic material behavior tend to cause large model-form errors. Applying “knock-down factors” to loads corresponding to bifurcation points to compensate for the shortcomings of linear models may not guarantee a reliable estimate of the margin of safety in all cases.

10. A Framework for explainable simulation

To satisfy the technical requirements of Explainable Artificial Intelligence in engineering, a simulation process must control three types of error: model-form, discretization, and calibration. The constraints

embedded in the formulation, together with the limits on the available calibration data, define the domain of calibration. Operating within this domain ensures decision-grade predictive reliability.

The estimation and control of both model-form and discretization errors rely on the definition of modeling and discretization hierarchies. This hierarchical structure enables traceability of modeling assumptions, allowing practitioners to attribute changes in the QoIs to specific modeling choices—a key requirement for explainability. For example, a model based on linear elasticity is a special case of a geometrically nonlinear model, which in turn is a special case of a formulation that accounts for material nonlinearities. Because boundary conditions and material constitutive laws can be represented in multiple ways, model hierarchies typically have multiple branches. This provides great flexibility in model definition, at the expense of having to identify one of the simplest models in the hierarchy that reliably captures all physical phenomena that significantly affect the QoIs.

The high-level workflow for explainable numerical simulation is structured as follows:

- **Formulate the mathematical model:** Relying on experience and insight, formulate a mathematical model that maps inputs to the QoIs. Although this formulation is strongly influenced by subjective judgment, viewing it as part of a hierarchical sequence of models provides a means to evaluate how modeling assumptions affect the QoIs. This perspective establishes an objective framework for identifying a model suitable for its intended application. Achieving this requires controlling discretization errors. Without such control, model-form errors may be masked by numerical errors.
- **Estimate and control numerical errors:** Construct a sequence of finite element spaces (via mesh refinement, polynomial *p*-extension, or both) and obtain a convergent sequence of finite element solutions. The QoIs, computed from this sequence, will approach an asymptotic limit. This limit provides an estimate of their exact values. Ideally, the discretization sequence is designed based on the expected regularity of the exact solution, as inferred from the input data.
- **Define the domain of calibration:** This entails assembling calibration data and performing calibration experiments to ensure that the domain of calibration is consistent with the intended application of the model. Establish limits for all operational inputs, boundary conditions, and material parameters for which the model has been validated.
- **Create the documentation:** Provide explicit statements of all assumptions incorporated in the model and the consequent limitations in scope. Indicate the sensitivity of the QoIs to specific modeling choices.

Adopting this structured approach transforms the simulation from an opaque "black-box" prediction into a transparent, verifiable process. This directly satisfies the technical requirements of engineering XAI.

Importantly, this framework accommodates the evolutionary, open-ended nature of mathematical model development. As available calibration data increase over time and operator formulations may be revised at any stage, model development processes must be adaptable [3].

11. Outlook

AI-assisted simulation technology is poised to deliver substantial benefits across engineering disciplines. In mechanical and structural engineering, it can enhance safety, improve reliability, and accelerate the introduction of new material systems.

A key development will be the emergence of AI systems that act as intelligent intermediaries between mathematical models and engineering practice. These systems will not replace expert judgment but will augment it by providing informed guidance during the execution of numerical simulations. By systematically accounting for model-form and discretization errors, they will be able to identify potential risks, such as using input data outside the calibration domain or discretizations that fail to meet prescribed error tolerances. Ensuring transparency and trust in these systems will require clear delineation of knowledge limits through the domains of calibration, in line with the technical requirements of XAI.

In addition, AI can assist in designing finite element discretizations by estimating the regularity of the exact solution from information contained in the input data and adaptively modifying the discretization based on feedback. Ideally, one or two adaptive steps should be sufficient. This capability can significantly accelerate the numerical solution process while maintaining accuracy.

Realizing the full potential of AI-integrated simulation will require substantial changes to existing finite element modeling software. As illustrated in this paper, incorporating hierarchical structures to control both model form and discretization errors is essential. This will also necessitate a shift from intuition-driven engineering practices toward methodologies grounded in the science of finite element analysis.

References

[1] Phillips, P. J., Hahn, C. A., Fontana, P. C., Yates, A. N., Greene, K., & Przybocki, M. A. (2021). *Four Principles of Explainable Artificial Intelligence* (NISTIR 8312). National Institute of Standards and Technology, 2021. https://doi.org/10.6028/NIST.IR.8312

[2] Mersha, M., Lam, K., Wood, J., Alshami, A.K., and Kalita, J. (2024). Explainable artificial intelligence: A survey of needs, techniques, applications, and future direction. *Neurocomputing*, *599*, p. 128111.

[3] Szabó, B. and Actis, R. (2024). The Demarcation Problem in the Applied Sciences. Computers and Mathematics with Applications. 162 pp. 206–214.

[4] Morgenstern, D. (1959). Herleitung der Plattentheorie aus der dreidimensionalen Elastizitätstheorie. *Archive for Rational Mechanics and Analysis*, *4*(1), pp. 145-152.

[5] Braess, D., Sauter, S., and Schwab, C. (2011). On the Justification of Plate Models. *Journal of Elasticity*, *103*(1), pp. 53-71.

[6] Przemieniecki, J. S. (Principal Editor) Matrix Methods in Structural Mechanics: Proceedings of the Conference Held at Wright-Patterson Air Force Base, Ohio, 26–28 October 1965, AFFDL-TR-66-80.

[7] Kuhn, T. S. (1997). *The structure of scientific revolutions* (Vol. 962). University of Chicago Press.

[8] Szabó, B. and Babuška, I. (2021). Finite Element Analysis. Method, Verification, and Validation. John Wiley & Sons Inc. Hoboken, NJ.

[9] Dauge, M. and Suri, M. (2002). Numerical approximation of the spectra of non-compact operators arising in buckling problems. *Journal of Numerical Mathematics*, vol. 10, no. 3, pp. 193-219. https://doi.org/10.1515/JNMA.2002.193

[10] Timoshenko, S. P. and Gere, J. M. (1961). Theory of Elastic Stability. McGraw-Hill Book Company, New York.

[11] Chen, Q. and Babuška, I. (1995). Approximate optimal points for polynomial interpolation of real functions in an interval and in a triangle. *Computer Methods in Applied Mechanics and Engineering*, *128*(3-4), pp. 405-417.

[12] Babuška, I. and Osborn, J. E. (1991). Eigenvalue Problems. In Handbook of Numerical Analysis, Vol. II (P. G. Ciarlet and J. L. Lions, eds.), North-Holland, pp. 641–787.

[13] Ortega, J. M. and Rheinboldt, W. C. (1970). Iterative Solution of Nonlinear Equations in Several Variables. Academic Press, New York.

[14] Riks, E. (1972). An incremental approach to the solution of snapping and buckling problems. *International Journal of Solids and Structures*. 15(7), 529–551.

[15] Hutchinson, J.W. (2016). Buckling of spherical shells revisited. *Proceedings of the Royal Society A: Mathematical, Physical and Engineering Sciences*, 472(2195), p.20160577.